

Bifurcation of time crystals in driven and dissipative Rydberg atomic gas

Received: 27 February 2024

Accepted: 28 January 2025

Published online: 06 February 2025



Bang Liu^{1,2}, Li-Hua Zhang^{1,2}, Yu Ma^{1,2}, Qi-Feng Wang^{1,2}, Tian-Yu Han^{1,2}, Jun Zhang^{1,2}, Zheng-Yuan Zhang^{1,2}, Shi-Yao Shao^{1,2}, Qing Li^{1,2}, Han-Chao Chen^{1,2}, Guang-Can Guo^{1,2}, Dong-Sheng Ding^{1,2}  & Bao-Sen Shi^{1,2} 

A time crystal is an exotic phase of matter where time-translational symmetry is broken; this phase differs from the spatial symmetry breaking induced in conventional crystals. Lots of experiments report the transition from a thermal equilibrium phase to a time crystal phase. However, there is no experimental method to probe the bifurcation effect of distinct continuous time crystals in quantum many-body systems. Here, in a driven and dissipative many-body Rydberg atom system, we observe multiple continuous dissipative time crystals and emergence of more complex temporal symmetries beyond the single time crystal phase. Bifurcation of time crystals in strongly interacting Rydberg atoms is observed; the process manifests as a transition from a time crystal of long periodicity to a time crystal of short periodicity, or vice versa. By manipulating the driving field parameters, we observe the time crystal's bistability and a hysteresis loop. These investigations indicate new possibilities for control and manipulation of the temporal symmetries of non-equilibrium systems.

The term time crystal refers to a unique state of matter in which a system exhibits spontaneous breaking of its time translation symmetry; this state was initially proposed by Frank Wilczek¹. In other words, the time crystal is a phase of matter in which the system's behavior repeats periodically in time. A time crystal exhibits long-range order in time, whereas conventional crystals exhibit long-range order in space. The state includes discrete and continuous time crystal phases^{2–5} that exhibit discrete and continuous time-translation symmetry breaking, respectively. Since the initial proposal, time crystals were first reported in experiments using trapped ions⁶ and the nitrogen-vacancy centers in diamonds⁷. There has been considerable progress on both the theoretical^{8–14} and experimental fronts in efforts to study and understand time crystals^{15–21}. Researchers continue to strive to improve the stability²² and the coherence^{23,24} of time crystals and to probe the equilibrium of quantum matter²⁵. Interestingly, the system comes out of thermal equilibrium dissipation under external driving conditions, and researchers have observed stabilized

dissipative time crystals²⁶, prethermal discrete time crystals^{27,28}, and higher-order time crystals^{29,30}.

The large dipole moment of the Rydberg atom provides a good platform for the study of the dynamics of strongly correlated systems. For example, researchers have used Rydberg atoms to probe quantum phase transitions^{31,32}, quantum scars^{33,34}, non-equilibrium phase transitions, and self-organized criticality^{35–40}. In traditional equilibrium systems, the second law of thermodynamics dictates that entropy will always increase with time, and this leads to thermal equilibrium and the absence of persistent oscillatory behavior. In the driven and dissipative Rydberg system, however, the external driving force injects energy into the system, while the long-range interactions between the system's constituents aid in redistributing this energy and thus help to maintain a persistent oscillatory evolution of the Rydberg atom population, and generating dissipative continuous time crystal⁴¹. In driven and dissipative Rydberg atoms systems, it is possible to observe some special matter phases, such as ergodic breaking^{42,43}, and the

¹Key Laboratory of Quantum Information, University of Science and Technology of China, 230026 Hefei, Anhui, China. ²Synergetic Innovation Center of Quantum Information and Quantum Physics, University of Science and Technology of China, 230026 Hefei, Anhui, China. ✉e-mail: dds@ustc.edu.cn

exotic emergence and transition dynamics of distinct continuous time crystals are worthy of study^{44,45}.

In this work, we observe a bifurcation effect for the continuous time crystals in strongly interacting Rydberg atoms under external radio-frequency (RF)-field continuous driving. The bifurcation of time crystals in Rydberg atoms originates from the competition between the excitations of different Floquet sidebands. Coupling between the (multiple) many-body states leads to the formation of distinct time crystals, which subsequently results in the emergence of more complex temporal symmetries beyond the simple discrete-time translation symmetry. We observe the full phase diagram of the system, including multiple distinct time crystal phases with several periodicities and chaotic phases. In addition, we observe phase transitions between the distinct time crystals and the hysteresis loop. Study of the emergence of these distinct time crystals will provide new possibilities for the exploration of the dynamics and control of quantum many-body systems when out of equilibrium.

Results

Physical model and experiment setup

To determine the time translation symmetry-breaking mechanism in driven and dissipative Rydberg atoms, we construct a simplified physical model that considers N interacting two-level atoms with a ground state $|g\rangle$ and the Rydberg state $|R\rangle$ (with a decay rate γ) to simulate the observations. A laser couples the atoms with a Rabi frequency Ω and detuning Δ . The Rydberg atoms are affected by the many-body interaction strength $V = C_6/r^6$ [where C_6 is the van der Waals coefficient and r represents the distance between the Rydberg atoms]. These atoms are exposed to an external RF field with an electric field component E_{RF} and frequency ω . The RF field perturbs the system and induces additional frequencies into the system spectrum, thus leading to the appearance of RF sidebands of the Rydberg states⁴⁶; see the Supplementary Information for further details. In our model, we consider the ± 1 -order sidebands of the Rydberg states as $|R_{1,2}\rangle$ with the corresponding Rabi frequency $\Omega_{1,2}$ and detuning $\Delta_{1,2}$. We use a mean field treatment to simulate multiple periodic oscillations in the Rydberg

atom population through master equation in Eq. (1); see the “Methods” section for further details.

In the experiments, we excite cesium atoms in a thermal vapor to study the features of time crystals. The cesium atom energy level structure and the experimental setup are depicted in Fig. 1a and b, respectively. We use a three-photon electromagnetically induced transparency (EIT) scheme to prepare the Rydberg atoms, as described in the previous study^{47,48}. Specifically, the excitation process involves using an 852 nm probe beam to resonantly drive the transition from state $|6S_{1/2}\rangle$ to state $|6P_{3/2}\rangle$ with a Rabi frequency Ω_p , a resonant 1470 nm laser with a Rabi frequency Ω_d to drive the transition from state $|6P_{3/2}\rangle$ to state $|7S_{1/2}\rangle$, and a 780 nm coupling beam with a Rabi frequency Ω_c and detuning Δ_c to drive the transition from state $|7S_{1/2}\rangle$ to $|49P_{3/2}\rangle$. The Rydberg atoms are illuminated by the RF field (the AC stark effect for the atomic state with the low principal quantum number can be ignored in this case). By tuning the system's parameters, we can observe the distinct continuous time crystals, which exhibit oscillated excitation rates from ground to Rydberg state, as shown in Fig. 1c and d. These are from the limit cycle phase under ergodicity breaking⁴², manifesting as persistent oscillations in phase space, as described in the physical model section (also predicted in Supplementary Fig. 3f). These oscillations can be persisted for at least a few minutes in the experiment, which is limited by the measurement time of the oscilloscope.

Figure 1c represents the time crystal of short periodicity (SP) and Fig. 1d represents the time crystal of long periodicity (LP). They are similar time crystals but with different frequencies. The oscillations of the time crystal are at a few to a few tens of kHz. In addition, we present evidence of a random phase distribution in these distinct time crystals. By measuring the dominant frequency peak f in the Fourier spectrum from the repeated trials (see further details in Supplementary Information), we obtain the distribution of the Fourier amplitudes in the complex plane. We performed 45 repeated measurements and a 1 s duration between the nearest measurements. Due to the drift of the peak frequency, we selected the data with the same peak frequency among the 45 sets of data and extracted the phase and amplitude of

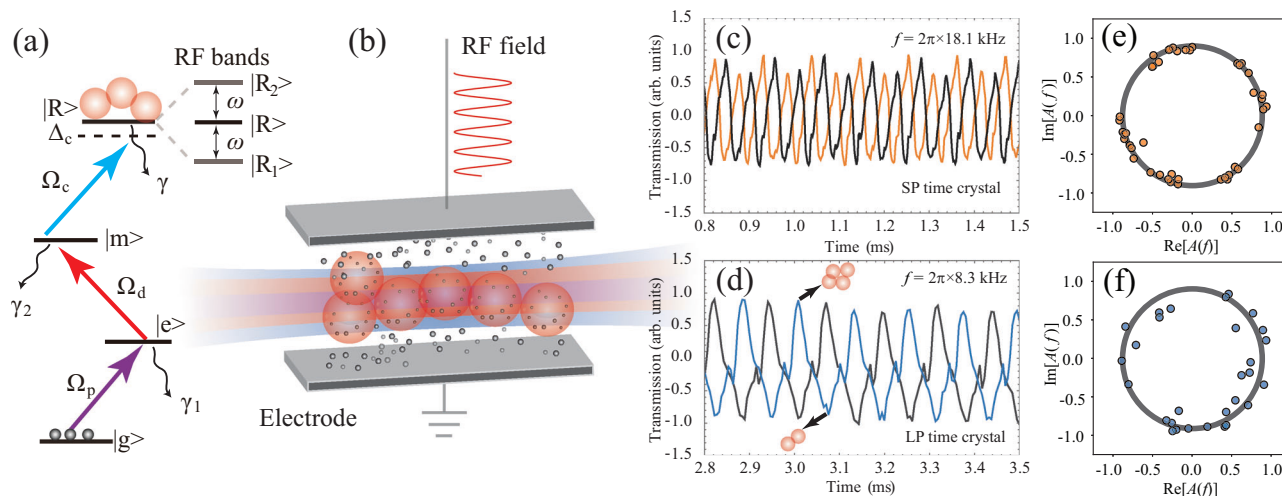


Fig. 1 | Energy level diagram and experimental setup for time crystal measurement. **a** Energy level diagram based on three-photon Rydberg electromagnetically induced transparency (EIT) scheme. γ_1 , γ_2 , and γ correspond to the decay rates of states $|e\rangle$, $|m\rangle$, and $|R\rangle$, respectively. The Rydberg state $|R\rangle$ is divided into Floquet sidebands when atoms are driven by an RF field; three sideband energy levels, $|R\rangle$, $|R_1\rangle$, and $|R_2\rangle$ with energy interval ω , are illustrated. **b** Simplified experimental setup. An RF field is applied to the atoms by two electrodes with a loading frequency ranging from 0 MHz - $2\pi \times 30$ MHz. **c** and **d** Triggered probe transmission within 0.7 ms time interval caused by switching on the RF field [$U = 3.8$ V], which oscillates with distinct frequencies [$f = 2\pi \times 18.1$ kHz (**c**) and

$f = 2\pi \times 8.3$ kHz (**d**)] obtained by setting $\Delta_c = -2\pi \times 24.1$ MHz for (**c**) and $\Delta_c = -2\pi \times 32.4$ MHz for (**d**), thus revealing the distinct time crystals. The different colored lines in **c** and **d** are from different experimental trials. The dips and peaks of oscillations correspond to the low and high density of excited Rydberg atoms [marked by different numbers of circles in (**d**)]. **e**, **f** Distributions of the Fourier amplitudes with the dominant frequency on the complex plane. In this process, we recorded the probe transmission within the time intervals $\Delta t = 0.7$ ms with 300 data points after the RF-field is turned on for **e** 0.8 ms and **f** 2.8 ms. The signal in **f** appears to be noisier than in **e** because the signal has more low-frequency noise.

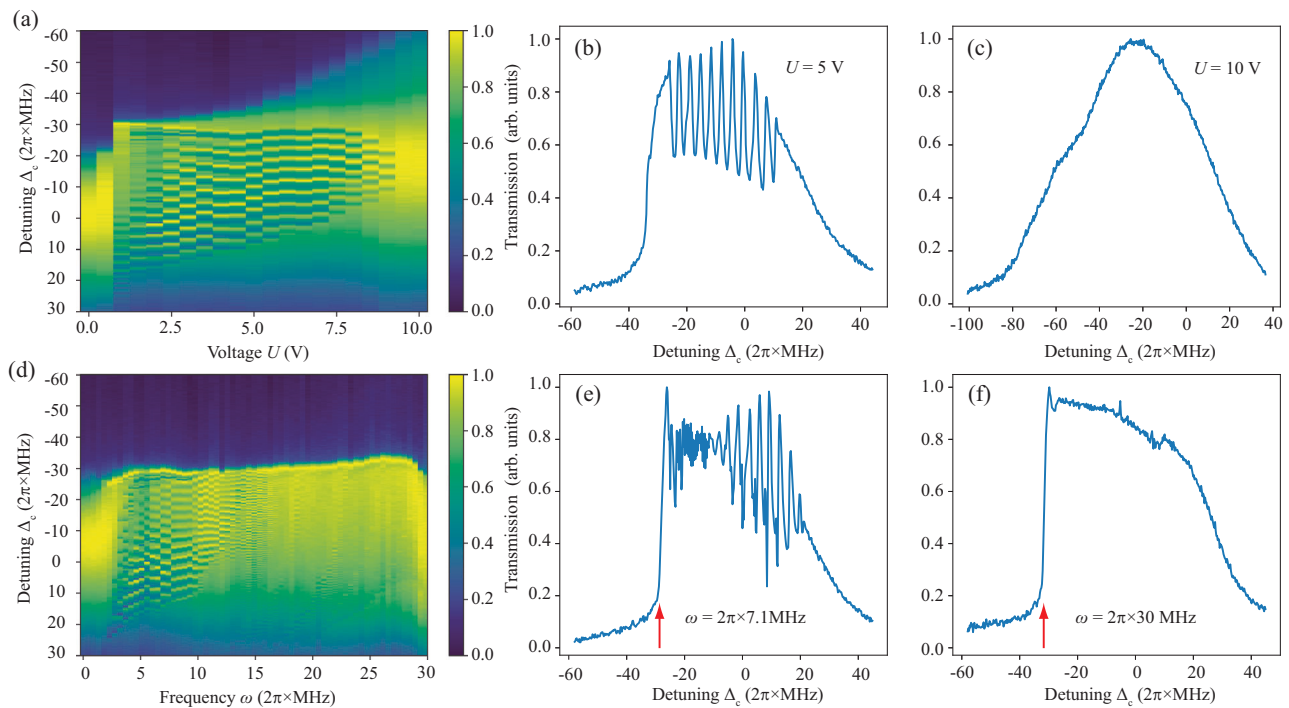


Fig. 2 | Measured phase diagram. Color maps of probe transmission (normalized with respect to their respective maximal values) when scanning Δ_c and the external RF field voltage U from 0 to 10 V (a), and the external RF field frequency ω from 0 to $2\pi \times 30$ MHz (d). Here, the coupling detuning Δ_c is scanned from $\Delta_c = -2\pi \times 60$ MHz to $\Delta_c = 2\pi \times 30$ MHz. In the oscillating regions in panels a and d, the system is in the time translation symmetry-breaking phase. The color bar ranging from 0 to 1 represents the transmission intensity. b and c correspond to

probe transmissions with $U = 5$ V and $U = 10$ V, respectively. Here, the RF field is set at $\omega = 2\pi \times 7.2$ MHz. e and f are the probe transmissions with RF field frequencies of $\omega = 2\pi \times 7$ MHz and $\omega = 2\pi \times 28$ MHz, respectively. The voltage is set $U = 2$ V. The red arrows shown in e and f indicate sudden jumps in the probe transmission spectrum, which are called non-equilibrium phase transitions. In panels b and e, oscillation behavior occurs in the probe transmission spectrum that corresponds to the non-trivial regime for time translation symmetry breaking.

the oscillations. The phase of the Fourier amplitude $A(f)$ at the dominant frequency f is distributed randomly between 0 and 2π , as shown in Fig. 1e and f, thus indicating spontaneous breaking of the continuous time translation symmetry⁴.

Phase diagram

To probe the exotic phase in the Rydberg atoms under RF field driving conditions, we measured the system's phase diagram. The phase diagram provides a comprehensive map of the different phases or states in which the transmission can exist as a function of various parameters, e.g., the coupling detuning Δ_c , voltage U , and frequency ω of the RF field. We varied the RF field intensity by varying the voltages of the electrodes and measured the probe transmission versus the coupling detuning Δ_c . Figure 2a shows the color map of the probe transmission when $U = 0$ –10 V and $\Delta_c = -2\pi \times 60$ MHz– $2\pi \times 30$ MHz. Figure 2b and c show examples of the probe transmission at $U = 5$ V and $U = 10$ V, respectively. We also changed the frequency of the RF field from $\omega = 0$ MHz to $\omega = 2\pi \times 30$ MHz and recorded the probe transmission, with results as shown in Fig. 2d. In the range of oscillation, the oscillation frequency increase versus with ω , which is consistent with the theoretical simulations in Supplementary Fig. 4b. Figure 2e and f show the corresponding results with $\omega = 2\pi \times 7$ MHz and $\omega = 2\pi \times 28$ MHz, respectively.

From these results, we found that oscillation effects occurred approximately within the range of $U = 0.7$ V– $U = 9.0$ V (Fig. 2a) and $\omega = 2\pi \times 2$ MHz– $\omega = 2\pi \times 16$ MHz (Fig. 2d). These results are also qualitatively predicted by the theories given by Supplementary Fig. 4b and c, in which time crystals appear and then disappear with the increase of parameters δ and $\Omega_{1/2}$. For example, in Fig. 2b, the system response exhibits repetitive back-and-forth motion on probe transmission at around resonance, whereas no oscillation is shown in Fig. 2c.

In Fig. 2a, the area of the oscillation covers a large coupling detuning when $U = 1$ V, but becomes narrower with increasing voltage U . Above $U = 9$ V, the probe transmission becomes non-oscillatory. The oscillation's disappearance at high U and high-frequency ω can be attributed to: (i) the high-intensity RF field inducing broadening larger than the shift from the Rydberg atom interactions; and (ii) the RF-field-induced Floquet energy interval (which is proportional to ω) being larger than the shift from the Rydberg atom interactions at high ω . In addition, there are sudden jumps indicated by red arrows in Fig. 2e and f. These jumps are bistability phase transition³⁷, in which the broadening effect induced by the RF field enables facilitated excitation of the Rydberg atoms.

Distinct time crystal phases

To study the characteristics of the time crystal phases in our system, we measured the Fourier spectrum of the oscillated transmission, as shown in Fig. 3a. There are comb-shaped spectra and chaotic spectra distributed in the varied Δ_c , which are separated within areas A–E. In area A, we see that the first peak ($f = f_0$) of the Fourier spectrum is nearly linear versus the coupling detuning Δ_c . In area B, the frequency of the time crystal remains stable versus varying Δ_c ; see the peak in Fig. 3b. These dynamics in these two regimes are also predicted qualitatively in Supplementary Fig. 4a in Supplementary Information. Interestingly, the time crystal becomes bifurcated when Δ_c is increased further. For example, a non-integer multiple of the f_0 frequency signals appears in areas C and D. In Fig. 3c and d, there are a series of branches at $f = f_0/4$, $f_0/2$, $3f_0/4$, $5f_0/4$, $3f_0/2$, and $7f_0/4$ at around $f = f_0$ in the Fourier spectrum. The appearance of multiple time crystals can be also predicted in our theory, they exhibit intertwined trajectories in phase space, see Supplementary Fig. 3 in Supplementary Information.

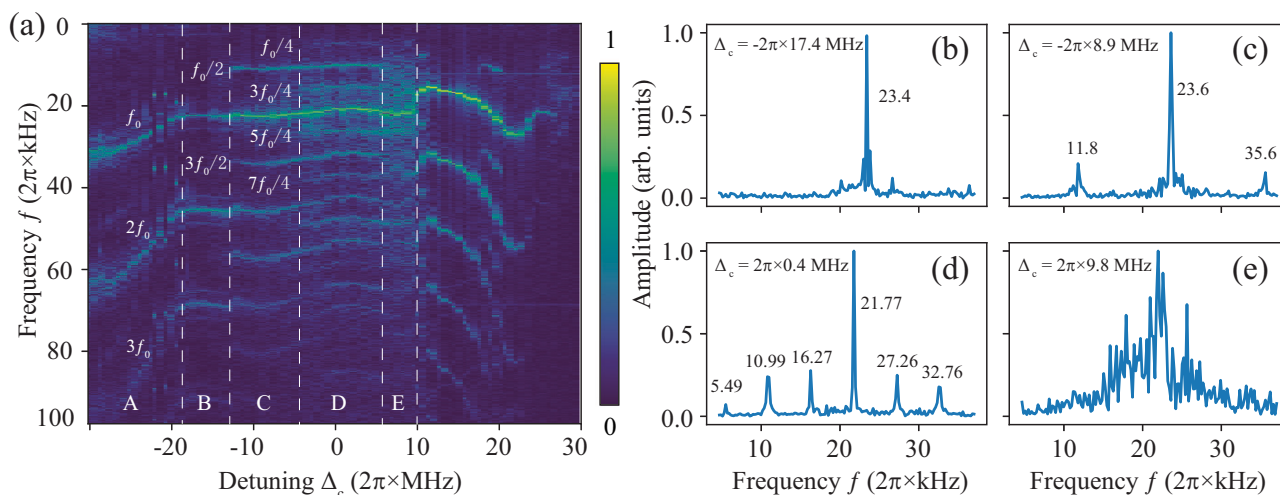


Fig. 3 | Distinct time crystals. **a** Measured Fourier spectrum versus the coupling detuning Δ_c . Labels A–E in **a** indicate the areas that characterize the distinct time crystal phases. The measured responses of several non-integer multiples of $f=f_0$ represent the ‘high-order’ continuous time crystals relative to the $f=f_0$ time crystal, which are the results of period doubling of f_0 peak. The color bar from 0 to 1 represents the Fourier transform intensity. **b–e** is the corresponding Fourier

spectrum at the detuning $\Delta_c/2\pi = -17.4 \text{ MHz}$ (**b**), $\Delta_c/2\pi = -8.9 \text{ MHz}$ (**c**), $\Delta_c/2\pi = -1.3 \text{ MHz}$ (**d**), and $\Delta_c/2\pi = 9.8 \text{ MHz}$ (**e**), respectively. The peaks in Fourier spectra **b–d** show evidence of distinct periodicity, and **e** is the measured Fourier spectrum of the chaotic phase. The sideband peaks that appeared close to f_0 are from the other small weighted oscillation modes.

The emergence of the non-integer multiple of $f=f_0$ frequency signals indicates the transition to a new temporal order. Increasing the coupling detuning from $\Delta_c = -2\pi \times 30 \text{ MHz}$ to $\Delta_c = -2\pi \times 0 \text{ MHz}$ adds to the population of Rydberg atoms and thus increases the interactions between the Rydberg atoms. The experimental observation is consistent with the phenomenon of period-doubling bifurcation in classical nonlinear dynamics⁴⁹. This is due to the fact that the stability of the phase space trajectory changes as the parameter Δ_c is varied, see Supplementary Fig. 3 in Supplementary Information.

By increasing Δ_c even further [e.g., to $\Delta_c = 2\pi \times 6 \text{ MHz}$], the system enters a chaotic regime in which the time crystals bifurcate further; see the relatively chaotic frequency spectrum in area E. Fig. 3e shows an example of the Fourier spectrum in area E. The bifurcation leads to the formation of additional temporal order patterns and the breakdown of the existing temporal order. This causes the excitation of the Rydberg atoms to be far from synchronized. As a result, the system may show more complex and unpredictable dynamics, along with the emergence of new frequency components and irregular oscillations. By varying the system parameter Δ_c , we observe the phenomenon of period-doubling bifurcation and the system finally goes to chaos. The phase space trajectory of the system becomes more and more chaotic, which ultimately leads to chaos, i.e., the satisfying of ergodicity. When $\Delta_c > 2\pi \times 10 \text{ MHz}$, the system response regains a single frequency oscillation and higher harmonic components as the interactions become weak. In this region, the oscillation frequency varies with respect to the change of Δ_c , similar to region A.

Phase transition of time crystal

We also measured the response versus the RF field intensity and mapped the phase diagram of the voltage range from 975 to 990 mV (see Fig. 4a), and this diagram illustrates two stable time crystals with different periodicities and the phase transition between them. When the voltage is in the $975 \text{ mV} < U < 982.5 \text{ mV}$ range, the system has a low-frequency time crystal phase. For example, we measured the Fourier spectrum at $U = 978.75 \text{ mV}$; there was a low-frequency peak at $f = 2\pi \times 19.0 \text{ kHz}$, as shown in Fig. 4b. With increasing voltage U , we found that the onset of the high-frequency time crystal phase appears on exceeding the critical voltage $U = 982.5 \text{ mV}$. The low-frequency component in the Fourier spectrum then disappears, and the high-

frequency term remains when we increase from $U = 975 \text{ mV}$ to $U = 990 \text{ mV}$; these results are shown in Fig. 4b–d.

Varying the RF field intensity causes the system’s symmetry to vary, and the probe transmission then shows distinct periodicity. The phase transition represents the system changing from an LP time-crystal into an SP time-crystal. We characterized the scaling of this phase transition using a fitting function; see the dashed line and the description in the caption of Fig. 4a. The modified Heaviside function displays the continuity of the spectrum. This supports a continuous transition from an LP time crystal to an SP time crystal.

Bistability of the time crystal

By scanning the RF field intensity in the forward and backward directions, we observed the bistability of the time crystal; the results are shown in Fig. 5a. Here, in the context of time crystals, bistability refers to the existence of two stable time crystal states or many-body energy levels that the Rydberg system can switch between. The upper panel in Fig. 5a corresponds to the measured phase diagram when the voltage U is increasing, and the lower panel in Fig. 5a shows the phase diagram measured when the voltage U is decreasing. When U is increased gradually, the time crystal phase is stable at a fixed frequency $f \sim 2\pi \times 11.64 \text{ kHz}$ within the range from $U = 3.5 \text{ V}$ to $U = 4.2 \text{ V}$. The frequency f corresponds to the largest peak in the spectrum of the system response and represents the dominant frequency component of the system response. Then, the system’s response shows a sudden jump when it crosses the critical point at $U = 4.2 \text{ V}$, and the system is then stable in another time crystal phase with a stable frequency of $f \sim 2\pi \times 16.93 \text{ kHz}$; see the results shown in Fig. 5b. Similarly, when U is gradually reduced, the time crystal phase switches at another entirely different critical point at $U = 3.95 \text{ V}$, as shown by the orange data in Fig. 5b.

The measured critical point voltages U during forward and backward scanning differ because of the dependence of the system on the initial state. This effect is often associated with the presence of non-equilibrium metastable states in the system where the system’s state does not reach a thermodynamic equilibrium. This comes from a non-ergodic effect⁴² and is also related to the hysteresis effect seen in refs. 36,37. This results in a delayed response in the RF field. This response lag leads to hysteresis and loop formation, as shown in Fig. 5b.

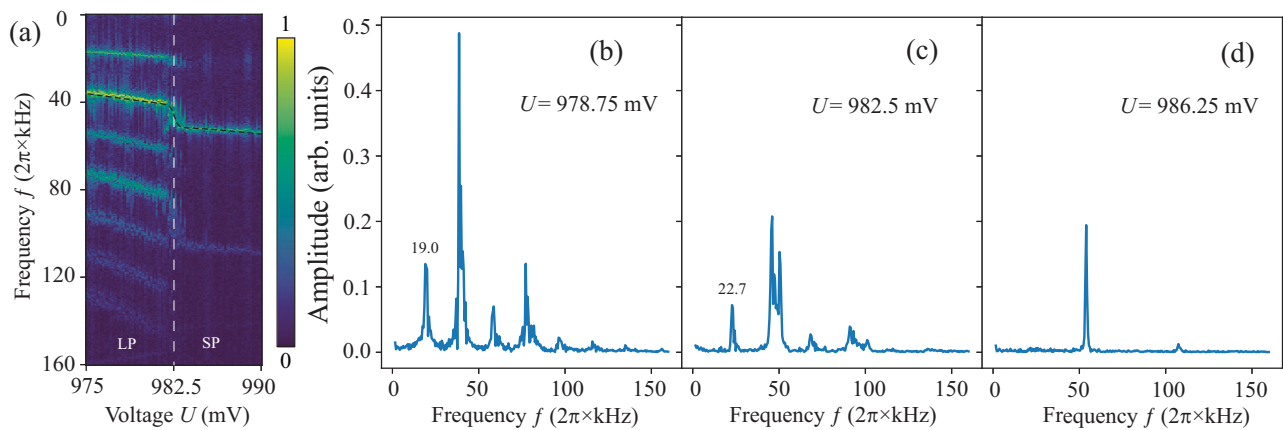


Fig. 4 | Phase transition between distinct time crystals. **a** Phase diagram of a voltage range from $U = 975$ mV to $U = 990$ mV in a high resolution. The black dashed line represents the modified Heaviside fitting function. The color bar from 0 to 1 represents the Fourier transform intensity. **b–d** Corresponding Fourier spectra at $U = 978.75$ mV (**b**), $U = 982.5$ mV (**c**), and $U = 986.25$ mV (**d**). The phase diagram

includes two temporal periodicities called the LP and the SP, which are separated by the white dashed line. In the SP time-crystal phase, the temporal order is the shorter-range order, which means that the system's response is repeated periodically over shorter time intervals. In the LP time-crystal phase, however, the system's response is repeated periodically over longer periods of time.

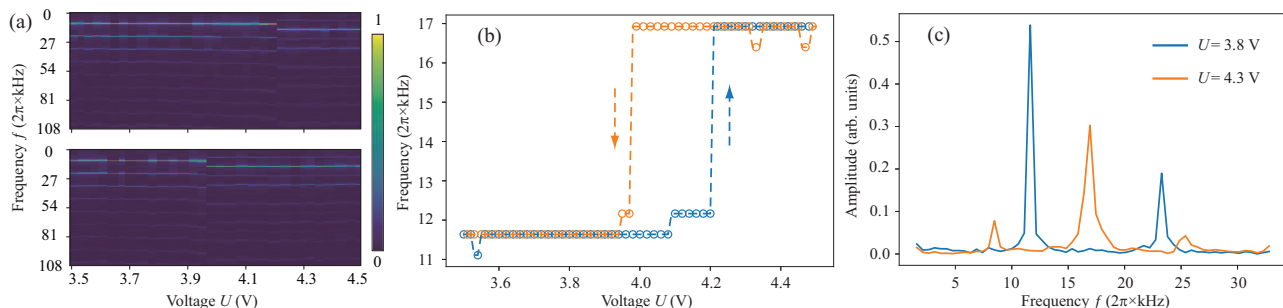


Fig. 5 | Bistability of time crystal. **a** Measured phase diagrams with forward scanning from $U = 3.5$ V to $U = 4.5$ V and vice versa. **b** Measured frequency of the dominant peak versus voltage U from (a). The blue data represents the forward scanning case and the orange data corresponds to the backward scanning case.

There is a hysteresis loop that indicates the relationship between the voltage U applied to the Rydberg atoms and the resulting dominant peak in the Fourier spectrum of the probe transmission. **c** Fourier spectra for $U = 3.8$ V (blue) and $U = 4.3$ V (orange).

Figure 5c illustrates the measured Fourier spectra of these two distinct time crystals.

Discussion

The observed time crystals are characterized using their nontrivial temporal orders, which represent the non-equilibrium persistent oscillations of the excited Rydberg atom population. There are no previous experimental reports observing the bifurcation effect of time crystals. The multiple time crystals and the bistability observed here open up avenues to study non-equilibrium physics with dependence on distinct temporal orders. Furthermore, the existence of multiple stable time crystal phases signifies a rich and diverse landscape for time crystal behavior^{2–5}. In addition, the RF field-driving technique plays an important role in creating more RF bands for the Rydberg state, thus providing a versatile method to obtain controllable many-body states.

Another interesting point is that the system transits from the time crystal phase to a chaotic phase during scanning of the voltage U , as depicted in area E in Fig. 3a or e. The irregular frequency distribution in Fig. 3e shows disordered properties that correspond to weak time translation symmetry breaking that results from imperfections in the orderly arrangement. We have simulated a nonlinear system using competitive interactions between Rydberg atoms and observed the phenomenon of period-doubling bifurcation. The period-doubling bifurcation that we observe experimentally is a common phenomenon

in nonlinear dynamics and an important path to chaos. Further study will allow us to deepen our understanding of complex systems as well as chaotic phenomena. Meanwhile, we can also use Rydberg atoms as a platform for simulating nonlinear dynamics to study nonlinear problems.

The distinct heights of the peaks in the Fourier spectrum (Figs. 3c and 4b) indicate that more than one time crystal exists under the same physical conditions in the system. This shows that the system could have multiple modes of time crystals. Because of the change in the interactions between the Rydberg atoms caused by Δ_c , it becomes possible to manipulate the system's ground state to be the coexistence of multiple time crystals with distinct f . This finding may be helpful in the study of the competition and time-dependence of many-body states.

In summary, we have demonstrated the bifurcation of time crystals in strongly interacting Rydberg atoms driven by an external RF field. Through this RF field-driving approach, we were able to observe the intriguing symmetry-breaking behavior of the time translation in Rydberg atoms. We observed multiple stable time crystals beyond the single time crystal within different coupling detuning ranges. By manipulating the RF field parameters, we observed a continuous phase transition from an LP state to an SP state and discovered the bistability of the time crystal, which manifested as a hysteresis loop. The bifurcation of the time crystal in strongly interacting Rydberg atoms is attributed to the emergence of more complex temporal symmetries

beyond the simple discrete time translation symmetry. Our work represents a milestone in understanding of the field of non-equilibrium transitions, and particularly with respect to the progression from a single time crystal phase to multiple distinct phases with different temporal symmetries.

Note: While finishing this manuscript we became aware of a related work of reporting a phase transition from a continuous to a discrete time crystal (ref. 44), and a related work (ref. 45) observing time crystal comb.

Methods

Experimental setup

The experimental details are depicted in Supplementary Fig. 1a. In the experiments, we used the three-photon scheme to excite the Rydberg atoms. The 852 nm external-cavity diode laser (ECDL) was locked by using the saturated absorption spectrum (SAS) as a frequency reference signal. Another ECDL at 1470 nm was locked by using the two-photon spectrum (TPS) as a frequency reference signal. The 780 nm ECDL was amplified using a tapered amplifier (TA) as a coupling laser. The probe laser is divided into two beams, where one beam serves as a reference, and the other beam propagates in the opposite direction to the dressing laser and coupling laser beams. We used the arbitrary function generator (AFG) to generate the RF field and apply it to the electrodes. The probe transmission was recorded using the oscilloscope after the signal passed through the photoelectric detector (PD). To scan the external parameters and thus obtain the phase diagram of the system response, the coupling laser, the oscilloscope, and the AFG were all connected to a computer and controlled together.

The probe light passes through a 7-cm vapor cell in parallel with the reference light, and the dressing light and the coupling light propagate backward from the probe light. The probe light is focused into the cell ($1/e^2$ -waist radius of approximately 200 μm) with a probe intensity of 64 μW . The dressing and coupling light are focused into the cell ($1/e^2$ -waist radius of approximately 500 μm) and the powers are 16.8 mW and 1.5 W, respectively. The Rabi frequencies of the probe light, dressing light, and coupling light are respectively $\Omega_p = 2\pi \times 35$ MHz, $\Omega_d = 2\pi \times 235$ MHz and $\Omega_c = 2\pi \times 4.3$ MHz. A pair of circular copper plates with a thickness of 3 mm and a diameter of $\Phi = 120$ mm were used in the experiment. The separation between the plates was adjusted to 40 mm and the Cesium cell was placed in the center of the plates.

Mean-field theory description

In our model, we consider N interacting four-level atoms with a ground state $|g\rangle$ and the Rydberg states $|R\rangle$, $|R_1\rangle$, and $|R_2\rangle$ (all with an equal decay rate γ). Here, a mean-field treatment was introduced to simulate the results. The system's master equation is based on the multi Rydberg-state model⁴¹:

$$\partial_t \hat{\rho} = i[\hat{H}, \hat{\rho}] + \mathcal{L}_R[\hat{\rho}] + \mathcal{L}_{R_1}[\hat{\rho}] + \mathcal{L}_{R_2}[\hat{\rho}] \quad (1)$$

where \hat{H} is the Hamiltonian and $\mathcal{L}_{\{R, R_1, R_2\}}$ is the Lindblad jump operator. The Hamiltonian of the system is

$$\begin{aligned} \hat{H} = & \frac{1}{2} \sum_i \left(\Omega \sigma_i^{gR} + \Omega_1 \sigma_i^{gR_1} + \Omega_2 \sigma_i^{gR_2} + h.c. \right) \\ & - \sum_i \left(\Delta n_i^R + \Delta_1 n_i^{R_1} + \Delta_2 n_i^{R_2} \right) \\ & + \sum_{i \neq j} \left[V_{ij}^{RR_1} n_i^R n_j^{R_1} + V_{ij}^{RR_2} n_i^R n_j^{R_2} + V_{ij}^{R_1 R_2} n_i^{R_1} n_j^{R_2} \right. \\ & \left. + \frac{1}{2} \left(V_{ij}^{RR} n_i^R n_j^R + V_{ij}^{R_1 R_1} n_i^{R_1} n_j^{R_1} + V_{ij}^{R_2 R_2} n_i^{R_2} n_j^{R_2} \right) \right] \end{aligned} \quad (2)$$

where σ_i^{gr} ($r = R, R_1, R_2$) represents the i th atom transition between the ground state $|g\rangle$ and the Rydberg state $|r\rangle$, n_i^{R, R_1, R_2} are the population operators of the Rydberg energy levels $|R\rangle$ and $|R_1\rangle$, and $|R_2\rangle$, and $V_{ij}^{RR_1}$, $V_{ij}^{RR_2}$, and $V_{ij}^{R_1 R_2}$ are the interactions between the Rydberg atoms in states $|R\rangle$, $|R_1\rangle$, and $|R_2\rangle$, respectively.

The Lindblad jump terms are given by

$$\mathcal{L}_r = (\gamma_r/2) \sum_i (\hat{\sigma}_i^{rg} \hat{\rho} \hat{\sigma}_i^{gr} - \{\hat{n}_i^r, \hat{\rho}\}), \quad (3)$$

which represents the decay process from the Rydberg state $|r\rangle$ ($r = R, R_1, R_2$) to the ground state $|g\rangle$.

In the mean-field treatment, we obtained the following equations:

$$\dot{\rho}_{RR} = i \frac{\Omega}{2} (\rho_{gR} - \rho_{Rg}) - \gamma \rho_{RR}, \quad (4)$$

$$\dot{\rho}_{R_1 R_1} = i \frac{\Omega_1}{2} (\rho_{gR_1} - \rho_{R_1 g}) - \gamma \rho_{R_1 R_1}, \quad (5)$$

$$\dot{\rho}_{R_2 R_2} = i \frac{\Omega_2}{2} (\rho_{gR_2} - \rho_{R_2 g}) - \gamma \rho_{R_2 R_2}, \quad (6)$$

$$\begin{aligned} \dot{\rho}_{gR} = & i \frac{\Omega}{2} (2\rho_{RR} + \rho_{R_1 R_1} + \rho_{R_2 R_2} - 1) + i \frac{\Omega_1}{2} \rho_{R_1 R} \\ & + i \frac{\Omega_2}{2} \rho_{R_2 R} + i(\Delta - \Delta_{int} + i\frac{\gamma}{2}) \rho_{gR}, \end{aligned} \quad (7)$$

$$\begin{aligned} \dot{\rho}_{gR_1} = & i \frac{\Omega_1}{2} (2\rho_{R_1 R_1} + \rho_{RR} + \rho_{R_2 R_2} - 1) + i \frac{\Omega}{2} \rho_{RR_1} \\ & + i \frac{\Omega_2}{2} \rho_{R_2 R_1} + i(\Delta_1 - \Delta_{int} + i\frac{\gamma}{2}) \rho_{gR_1}, \end{aligned} \quad (8)$$

$$\begin{aligned} \dot{\rho}_{gR_2} = & i \frac{\Omega_2}{2} (2\rho_{R_2 R_2} + \rho_{R_1 R_1} + \rho_{RR} - 1) + i \frac{\Omega}{2} \rho_{R_2 R} \\ & + i \frac{\Omega_1}{2} \rho_{R_1 R_2} + i(\Delta_2 - \Delta_{int} + i\frac{\gamma}{2}) \rho_{gR_2}, \end{aligned} \quad (9)$$

$$\dot{\rho}_{RR_1} = i \left(\frac{\Omega_1}{2} \rho_{gR_1} - \frac{\Omega_1}{2} \rho_{Rg} \right) - i(\Delta - \Delta_1 - i\gamma) \rho_{RR_1}, \quad (10)$$

$$\dot{\rho}_{RR_2} = i \left(\frac{\Omega_2}{2} \rho_{gR_2} - \frac{\Omega_2}{2} \rho_{Rg} \right) - i(\Delta - \Delta_2 - i\gamma) \rho_{RR_2}, \quad (11)$$

$$\dot{\rho}_{R_1 R_2} = i \left(\frac{\Omega_1}{2} \rho_{gR_2} - \frac{\Omega_2}{2} \rho_{R_1 g} \right) - i(\Delta_1 - \Delta_2 - i\gamma) \rho_{R_1 R_2}, \quad (12)$$

where $\Delta_1 = \Delta - \delta$, $\Delta_2 = \Delta + \delta$, $\Delta_{int} = \xi(\rho_{RR} + \rho_{R_1 R_1} + \rho_{R_2 R_2})$ is the interaction-induced shift, and ξ is the interaction coefficient. The δ is the energy spacing between the Rydberg states in the theoretical model. It corresponds to the frequency of the RF in the experimental system. According to Floquet's theory introduced in the "Methods" section, RF induces equally spaced sidebands in the Rydberg levels, so $\delta = \omega$. In this way, we can calculate the system's dynamics within the limit cycle regime.

Data availability

The data generated in this study have been deposited in the Zenodo database (<https://doi.org/10.5281/zenodo.13164754>).

Code availability

The custom codes used to produce the results presented in this paper are available from the corresponding authors upon request.

References

- Wilczek, F. Quantum time crystals. *Phys. Rev. Lett.* **109**, 160401 (2012).
- Sacha, K. & Zakrzewski, J. Time crystals: a review. *Rep. Prog. Phys.* **81**, 016401 (2017).
- Else, D. V., Monroe, C., Nayak, C. & Yao, N. Y. Discrete time crystals. *Annu. Rev. Condens. Matter Phys.* **11**, 467 (2020).
- Kongkhambut, P. et al. Observation of a continuous time crystal. *Science* **377**, 670 (2022).
- Zaletel, M. P. et al. Colloquium: quantum and classical discrete time crystals. *Rev. Mod. Phys.* **95**, 031001 (2023).
- Zhang, J. et al. Observation of a discrete time crystal. *Nature* **543**, 217 (2017).
- Choi, S. et al. Observation of discrete time-crystalline order in a disordered dipolar many-body system. *Nature* **543**, 221 (2017).
- Watanabe, H. & Oshikawa, M. Absence of quantum time crystals. *Phys. Rev. Lett.* **114**, 251603 (2015).
- Syrwid, A., Zakrzewski, J. & Sacha, K. Time crystal behavior of excited eigenstates. *Phys. Rev. Lett.* **119**, 250602 (2017).
- Huang, B., Wu, Y.-H. & Liu, W. V. Clean Floquet time crystals: models and realizations in cold atoms. *Phys. Rev. Lett.* **120**, 110603 (2018).
- Gong, Z., Hamazaki, R. & Ueda, M. Discrete time-crystalline order in cavity and circuit QED systems. *Phys. Rev. Lett.* **120**, 040404 (2018).
- Yao, N. Y., Nayak, C., Balents, L. & Zaletel, M. P. Classical discrete time crystals. *Nat. Phys.* **16**, 438 (2020).
- Nie, X. & Zheng, W. Mode softening in time-crystalline transitions of open quantum systems. *Phys. Rev. A* **107**, 033311 (2023).
- Gambetta, F., Carollo, F., Marcuzzi, M., Garrahan, J. & Lesanovsky, I. Discrete time crystals in the absence of manifest symmetries or disorder in open quantum systems. *Phys. Rev. Lett.* **122**, 015701 (2019).
- Li, T. et al. Space-time crystals of trapped ions. *Phys. Rev. Lett.* **109**, 163001 (2012).
- Else, D. V., Bauer, B. & Nayak, C. Floquet time crystals. *Phys. Rev. Lett.* **117**, 090402 (2016).
- Autti, S., Eltsov, V. & Volovik, G. Observation of a time quasicrystal and its transition to a superfluid time crystal. *Phys. Rev. Lett.* **120**, 215301 (2018).
- Smits, J., Liao, L., Stoof, H. & van der Straten, P. Observation of a space-time crystal in a superfluid quantum gas. *Phys. Rev. Lett.* **121**, 185301 (2018).
- Pizzi, A., Nunnenkamp, A. & Knolle, J. Bistability and time crystals in long-ranged directed percolation. *Nat. Commun.* **12**, 1061 (2021).
- Autti, S. et al. Ac Josephson effect between two superfluid time crystals. *Nat. Mater.* **20**, 171 (2021).
- Träger, N. et al. Real-space observation of magnon interaction with driven space-time crystals. *Phys. Rev. Lett.* **126**, 057201 (2021).
- Machado, F., Zhuang, Q., Yao, N. Y. & Zaletel, M. P. Absolutely stable time crystals at finite temperature. *Phys. Rev. Lett.* **131**, 180402 (2023).
- Rovny, J., Blum, R. L. & Barrett, S. E. Observation of discrete-time-crystal signatures in an ordered dipolar many-body system. *Phys. Rev. Lett.* **120**, 180603 (2018).
- Randall, J. et al. Many-body-localized discrete time crystal with a programmable spin-based quantum simulator. *Science* **374**, 1474 (2021).
- Ho, W. W., Choi, S., Lukin, M. D. & Abanin, D. A. Critical time crystals in dipolar systems. *Phys. Rev. Lett.* **119**, 010602 (2017).
- Keßler, H. et al. Observation of a dissipative time crystal. *Phys. Rev. Lett.* **127**, 043602 (2021).
- Vu, D. & Sarma, S. D. Dissipative prethermal discrete time crystal. *Phys. Rev. Lett.* **130**, 130401 (2023).
- Kyprianidis, A. et al. Observation of a prethermal discrete time crystal. *Science* **372**, 1192 (2021).
- Pizzi, A., Knolle, J. & Nunnenkamp, A. Period- n discrete time crystals and quasicrystals with ultracold bosons. *Phys. Rev. Lett.* **123**, 150601 (2019).
- Pizzi, A., Knolle, J. & Nunnenkamp, A. Higher-order and fractional discrete time crystals in clean long-range interacting systems. *Nat. Commun.* **12**, 2341 (2021).
- Bernien, H. et al. Probing many-body dynamics on a 51-atom quantum simulator. *Nature* **551**, 579 (2017).
- Keesling, A. et al. Quantum Kibble–Zurek mechanism and critical dynamics on a programmable Rydberg simulator. *Nature* **568**, 207 (2019).
- Serbyn, M., Abanin, D. A. & Papić, Z. Quantum many-body scars and weak breaking of ergodicity. *Nat. Phys.* **17**, 675 (2021).
- Bluvstein, D. et al. Controlling quantum many-body dynamics in driven Rydberg atom arrays. *Science* **371**, 1355 (2021).
- Lee, T. E., Haefner, H. & Cross, M. Collective quantum jumps of Rydberg atoms. *Phys. Rev. Lett.* **108**, 023602 (2012).
- Carr, C., Ritter, R., Wade, C., Adams, C. S. & Weatherill, K. J. Nonequilibrium phase transition in a dilute Rydberg ensemble. *Phys. Rev. Lett.* **111**, 113901 (2013).
- Ding, D.-S., Busche, H., Shi, B.-S., Guo, G.-C. & Adams, C. S. Phase diagram of non-equilibrium phase transition in a strongly-interacting Rydberg atom vapour. *Phys. Rev. X* **10**, 021023 (2020).
- Helmrich, S., Arias, A., Lochead, G., Wintermantel, T., Buchhold, M., Diehl, S. & Whitlock, S. Signatures of self-organized criticality in an ultracold atomic gas. *Nature* **577**, 481 (2020).
- Klocke, K., Wintermantel, T., Lochead, G., Whitlock, S. & Buchhold, M. Hydrodynamic stabilization of self-organized criticality in a driven Rydberg gas. *Phys. Rev. Lett.* **126**, 123401 (2021).
- Ding, D.-S. et al. Enhanced metrology at the critical point of a many-body Rydberg atomic system. *Nat. Phys.* **18**, 1447 (2022).
- Wu, X. et al. Dissipative time crystal in a strongly interacting Rydberg gas. *Nat. Phys.* **20**, 1389–1394 (2024).
- Ding, D. et al. Ergodicity breaking from Rydberg clusters in a driven-dissipative many-body system. *Sci. Adv.* **10**, ead15893 (2024).
- Wadenpfuhl, K. & Adams, C. S. Emergence of synchronization in a driven-dissipative hot Rydberg vapor. *Phys. Rev. Lett.* **131**, 143002 (2023).
- Kongkhambut, P. et al. Observation of a phase transition from a continuous to a discrete time crystal. *Rep. Prog. Phys.* **87**, 080502 (2024).
- Jiao, Y. et al. Observation of time crystal comb in a driven-dissipative system. arXiv preprint arXiv:2402.13112 (2024).
- Miller, S. A., Anderson, D. A. & Raithel, G. Radio-frequency-modulated Rydberg states in a vapor cell. *N. J. Phys.* **18**, 053017 (2016).
- Zhang, L.-H. et al. Rydberg microwave-frequency-comb spectrometer. *Phys. Rev. Appl.* **18**, 014033 (2022).
- Liu, B. et al. Highly sensitive measurement of a megahertz rf electric field with a Rydberg-atom sensor. *Phys. Rev. Appl.* **18**, 014045 (2022).
- Strogatz, S. H. *Nonlinear Dynamics and Chaos: with Applications to Physics, Biology, Chemistry, and Engineering* (CRC Press, 2018).

Acknowledgements

D.-S.D. thanks for the previous discussions with Prof. Igor Lesanovsky and Prof. C. Stuart Adams on time crystals. We acknowledge funding from the National Key R and D Program of China (Grant No. 2022YFA1404002), the National Natural Science Foundation of China (Grant Nos. U20A20218, T2495253, 61525504, and 61435011), the Anhui Initiative in Quantum Information Technologies (Grant No. AHY020200), and the Major Science and Technology Projects in Anhui Province (Grant No. 202203a13010001).

Author contributions

D.-S.D. conceived the idea for the study. B.L. conducted the physical experiments and developed the theoretical model. B.L. collected data with assistance of L.-H.Z., Y.M., T.-Y.H., and Q.-F.W., discussed data with J.Z., Z.-Y.Z., S.-Y.S., Q.L., H.-C.C., G.-C.G., and B.-S.S. The manuscript was written by D.-S.D. and B.L. The research was supervised by D.-S.D. All authors contributed to discussions regarding the results and the analysis contained in the manuscript.

Competing interests

The authors declare no competing interests.

Additional information

Supplementary information The online version contains supplementary material available at <https://doi.org/10.1038/s41467-025-56712-1>.

Correspondence and requests for materials should be addressed to Dong-Sheng Ding.

Peer review information *Nature Communications* thanks the anonymous reviewers for their contribution to the peer review of this work. A peer review file is available.

Reprints and permissions information is available at <http://www.nature.com/reprints>

Publisher's note Springer Nature remains neutral with regard to jurisdictional claims in published maps and institutional affiliations.

Open Access This article is licensed under a Creative Commons Attribution-NonCommercial-NoDerivatives 4.0 International License, which permits any non-commercial use, sharing, distribution and reproduction in any medium or format, as long as you give appropriate credit to the original author(s) and the source, provide a link to the Creative Commons licence, and indicate if you modified the licensed material. You do not have permission under this licence to share adapted material derived from this article or parts of it. The images or other third party material in this article are included in the article's Creative Commons licence, unless indicated otherwise in a credit line to the material. If material is not included in the article's Creative Commons licence and your intended use is not permitted by statutory regulation or exceeds the permitted use, you will need to obtain permission directly from the copyright holder. To view a copy of this licence, visit <http://creativecommons.org/licenses/by-nc-nd/4.0/>.

© The Author(s) 2025